Geophys. J. Int. (2004) **157,** 813–830 doi: 10.1111/j.1365-246X.2004.02265.x

Q tomography of the upper mantle using three-component long-period waveforms

Y. Gung and B. Romanowicz

Department of Earth and Planetary Science, and Seismological Laboratory, University of California at Berkeley, 215 *McCone Hall, Berkeley, CA* 94720-4760, *USA. E-mail: gung@seismo.berkeley.edu*

Accepted 2004 January 13. Received 2004 January 13; in original form 2003 July 24

SUMMARY

We present a degree-8 3-D *Q* model (QRLW8) of the upper mantle, derived from three-component surface waveform data in the period range 60–400 s. The inversion procedure involves two steps. In the first step, 3-D whole-mantle velocity models are derived separately for elastic *SH* (transverse component) and *SV* (vertical and longitudinal component) velocity models, using both surface and body waveforms and the non-linear asymptotic coupling theory (NACT) approach. In the second step, the surface waveforms thus aligned in phase are inverted to obtain a 3-D *Q* model in the depth range 80–670 km. Various stability tests are performed to assess the quality of the resulting *Q* model and, in particular, to assess possible contamination from focusing effects. We find that the 3-D patterns obtained are stable, but the amplitude of the lateral variations in *Q* is not well constrained, because large damping is necessary to extract the weak *Q* signal from data. The model obtained agrees with previous results in that a strong correlation of *Q* with tectonics is observed in the first 250 km of the upper mantle, with high attenuation under oceanic regions and low attenuation under continental shields. It is gradually replaced by a simpler pattern at larger depth. At the depths below 400 km, the *Q* distribution is generally dominated by two strong minima, one under the southern Pacific and one under Africa, yielding a strong degree-2 pattern. Most hotspots are located above regions of low *Q* at this depth. Ridges are shallow features in both velocity and *Q* models.

Key words: attenuation, upper mantle, waveform tomography.

1 INTRODUCTION

Resolving global 3-D anelastic structure in the mantle is important for at least two reasons:

(i) The quality factor *Q* of the earth is considerably more sensitive to temperature variations than the elastic velocity (e.g. Jackson *et al.* 1992), which implies that, in principle, *Q* tomography should be able to provide us with important information on the thermal structure in the mantle and therefore its dynamics, in complement to that provided by elastic tomography. In particular, it should help us to distinguish the distribution of chemical versus thermal heterogeneity in the mantle (Romanowicz 1995).

(ii) Attenuation causes dispersion in seismic velocities and this dispersion effect needs to be taken into account when interpreting velocity models (e.g. Romanowicz 1990; Karato 1993).

In the last two decades, global elastic tomography has made striking progress. Significant agreement is observed among 3-D whole-mantle elastic models derived by research groups using different modelling techniques and a variety of data sets [e.g. Woodhouse & Dziewonski (1984); Su *et al.* (1994); Li & Romanowicz (1996, hereafter referred to as LR96); Masters *et al.* (1996); Grand *et al.* (1997); van der Hilst *et al.* (1997); Vasco & Johnson (1998); Mégnin & Romanowicz (2000, hereafter referred to as MR00); Gu *et al.* (2001)]. In contrast, progress in anelastic tomography has been slow, because of the inherent technical difficulties encountered in extracting anelastic signals from amplitude data.

To date, only a few 3-D global attenuation models have been published. While several attempts at retrieving the distribution of even order heterogeneity in upper mantle *Q* have been made using normal mode data (Roult *et al.* 1990; Suda *et al.* 1991) or propagating Rayleigh wave data (Romanowicz 1990; Durek *et al.* 1993). The first complete 3-D *Q* model of the upper mantle, QR19, which includes both even and odd heterogeneities, provided lateral resolution equivalent to approximately degree 5 in a spherical harmonics expansion and remained largely qualitative (Romanowicz 1995). In that study, attenuation coefficients were measured in the spectral domain, for low-frequency(100–300 s) Rayleigh waves on multiple orbits, using a method designed to minimize the effects of focusing and scattering as a result of wave propagation in the complex 3-D elastic earth, as well as the effect of uncertainties in the source moment and radiation pattern. More recently, Billien *et al.* (2000) derived global Rayleigh

wave attenuation maps, from simultaneous inversion of phase and amplitude data. Selby & Woodhouse (2002) presented a set of 3-D Q_μ models of the upper mantle based on amplitude measurement of minor and major arc Rayleigh waves in the period range 70–170 s. Several authors have also developed methods to extract attenuation information from body wave data. Bhattacharyya *et al.* (1996) analysed differential *SS–S* waveforms using a multitaper frequency domain technique to measure the variation of attenuation in the upper mantle. Reid *et al.* (2001) applied a differential waveform-fitting method to multiple *S* phases (*SS–S* and *SSS–SS*), to constrain the elastic and anelastic structure of the mantle simultaneously. Warren & Shearer (2002) analysed *P* and *PP* spectra to map lateral variations in *P* wave attenuation in the top 220 km of the upper mantle. While the source effects are reduced in differential body wave amplitude measuring techniques, the depth resolution of the resulting models is limited.

Although the similarities between these global *Q* models are much less clear than those in global elastic models, there are several common features in the shallow mantle (depth < 250 km): low *Q* beneath active tectonic regions, high *Q* beneath stable shield regions and, in general, correlation between slow velocities and high attenuation. The *Q* variations are correlated with tectonic features in the shallow mantle.

In theory, waveform inversion techniques used in elastic tomography (e.g. Woodhouse & Dziewonski 1984, LR96) can be applied to anelastic tomography as well. However, the changes in waveforms as a result of elastic effects (focusing and scattering) are commensurate with those resulting from intrinsic attenuation, which makes it a challenge to isolate the attenuation effects on seismograms. To better identify these interfering effects, most *Q* measurements are usually made in the spectral domain (e.g. Romanowicz 1995; Bhattacharyya *et al.* 1996; Durek & Ekström 1996). The drawback of spectral approaches is that they require isolated phases on the seismograms, which limits the resolution that can be attained in the mantle.

In this study, we show that *Q* tomography based on waveform inversion is feasible, if reliable elastic models and careful data selection are utilized to minimize the interfering effects. We present the results of a global tomographic inversion for lateral variations in $Q\mu$ in the upper mantle, using a data set of three-component surface waves in the period range 60–400 s. Unlike our previous *Q* studies, in which measurements were performed in the spectral domain (e.g. Romanowicz 1990, 1995), the present modelling technique is based on the waveform methodology developed by Li & Romanowicz (1995) (hereinafter referred to as LR95), with appropriate modification to convert the code from elastic to anelastic inversion, and applied to three-component data.

We first describe the data set and the inversion procedure, explore the mutual influence of elastic and anelastic effects with a test inversion based on synthetic data and present a degree-16 V_{SV} mantle model, which will be used for phase correction in *Q* tomography of Rayleigh wave data. In order to account for significant transverse isotropy in the upper mantle (e.g. Montagner & Tanimoto 1990; Ekström & Dziewonski 1998; Gung *et al.* 2003), phase correction of Love wave data is based on a V_{SH} model, SAW24B16 (MR00). Then we present our final degree-8 *Q* model, QRLW8, derived after phase correction using Rayleigh and Love waveform data measured on all three components. Finally, we assess the model stability by various experiments. For the geodynamic implications of QRLW8, we refer the reader to Romanowicz & Gung (2002).

2 DATA

We restrict the modelling of 3-D *Q* variations to the upper mantle. The strong sensitivity of surface waves to the upper mantle makes them appropriate for this purpose.

Our surface wave data set is composed of two parts. The first part consists of fundamental mantle Love waves of the first and second orbits (*G*1 and *G*2), low-pass filtered with a cut-off frequency of 1/80 Hz and a corner frequency of 1/100 Hz. They were recorded on global networks for earthquakes occurring between 1977 and 1992. This hand-picked data set is a subset of the waveform data set used in the development of the degree-12 shear velocity model of the whole-mantle SAW12D (LR96) and the subsequent higher degree model SAW24B16 (MR00).

To further improve the coverage and depth resolution, we complemented this data set with newly processed waveforms, which, in addition to transverse component data(Love waves), include data from vertical and radial components (Rayleigh waves). Beside the fundamental waves of the first and second orbits, this data set also includes overtone phases. Events of magnitude greater than *Mw* 5.5 are considered. These new events were recorded at IRIS stations for 249 events for the period 1995–1999 and at Geoscope stations for 440 events for the time period 1993–1999. Fig. 1 shows the geographical distribution of events in the data set. All selected events are properly time isolated to avoid interference with other events. To prevent possible complications from the long source-time duration, very large events ($M_0 > 10^{20}$ Nm) are not used. Seismograms recorded near the epicenters or their antipodes ($\Delta < 15^\circ$ or $\Delta > 165^\circ$) are not selected, because the asymptotic theory breaks down near $\Delta = 0^\circ$ or $\Delta = 180^\circ$ (e.g. Romanowicz 1987).

Compared to the first data set, the second data set is low-pass filtered with higher cut-off frequency and corner frequency (1/60 and 1/80 Hz, respectively), in order to improve resolution in the shallow mantle.

In Fig. 2, we show the sensitivity of Love and Rayleigh waves to earth structure at periods of 100 and 200 s. Love waves are highly sensitive to shallow structure and Rayleigh waves provide constraints in the intermediate depth range of the upper mantle, complementary to the information provided by Love waves. Because the depth of peak sensitivity of fundamental Rayleigh waves increases significantly with increasing period, we expect that better depth resolution in the upper mantle can be obtained using a combination of Rayleigh and Love wave data.

We adopt the individual wave-packet technique first proposed by LR96. Compared with the more standard full trace approach, this wave-packet technique has the advantage of allowing us to assign weights to wave packets with different amplitudes, thereby preventing the inversion from being dominated by the data with the largest amplitudes (Mégnin & Romanowicz 1999). From the point of view of *Q* inversion, the wave-packet technique also guarantees more reliable amplitude information, because only those portions of data associated with major energy arrivals are selected.

To overcome the drawback of slow data acquisition with manual wave-packet picking, we developed an autopicking algorithm to gather a sufficient data set in a reasonable amount of time. While the original data set in LR96 was hand-picked, the second data set was collected using this algorithm. An example of the waveform data selected by autopicking is shown in Fig. 3. The complete data selection procedure is as follows:

(i) Compare the raw data with synthetics obtained by mode summation for a reference model combining elastic PREM

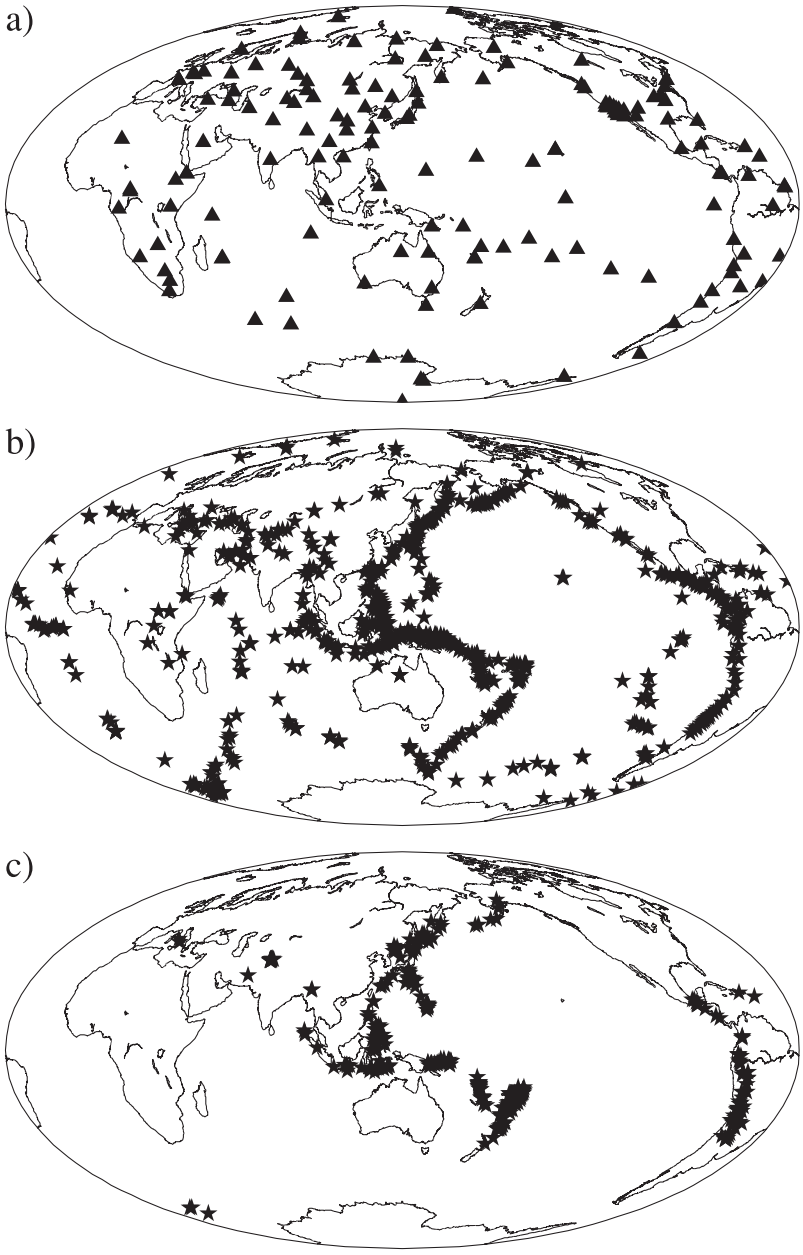

Figure 1. Distribution of stations and epicenters for this study: (a) stations; (b) shallow events (depth <100 km); (c) deep events (depth >100 km).

(Dziewonski & Anderson 1981) and anelastic QL6 (Durek & Ekström 1996). Noisy and glitchy traces are first eliminated. Approximately 25 per cent of vertical component and 60 per cent of transverse and longitudinal components of data traces available are rejected. Because of the noisy character of horizontal component records, more horizontal component data are rejected (Fig. 3).

(ii) The data trace is broken into individual wave packets of major energy arrivals. On a packet-by-packet basis, the variance residuals (normalized by data and synthetics, independently) and ratios between the maximum amplitude of observed and synthetics are used as criteria for data elimination. We reject data whose normalized variance is larger than 2, or whose amplitude ratio is larger than 2 or smaller than 0.5. These criteria allow us to remove wave packets that are noisy or strongly affected by unwanted effects, such as focusing or complex source process. Approximately 50 per cent of the wave packets are rejected at this stage.

(iii) The qualified data in the previous two steps are used in elastic tomography. Because phase alignment between observed and synthetic waves are important prior to Q inversion(detailed in Section 4), stricter data selection criteria based on waveform correlation are applied for the Q inversion. Specifically, we compare the waveform correlation between data and synthetics computed in the 3-D velocity models obtained in the first step, and reject data with correlation less than 0.5. As a result, approximately 30 per cent of data used in the velocity inversion are excluded from the following Q inversion.

The Q inversion uses 15 777 transverse (Love waves), 4820 radial and 10 770 vertical component (Rayleigh waves) wave packets. The coverage obtained with these data is shown in Fig. 4, where it is expressed as the logarithm of the sampling ray length (in degrees) in each 10° by 10° cell, corrected for latitude. To prevent images of

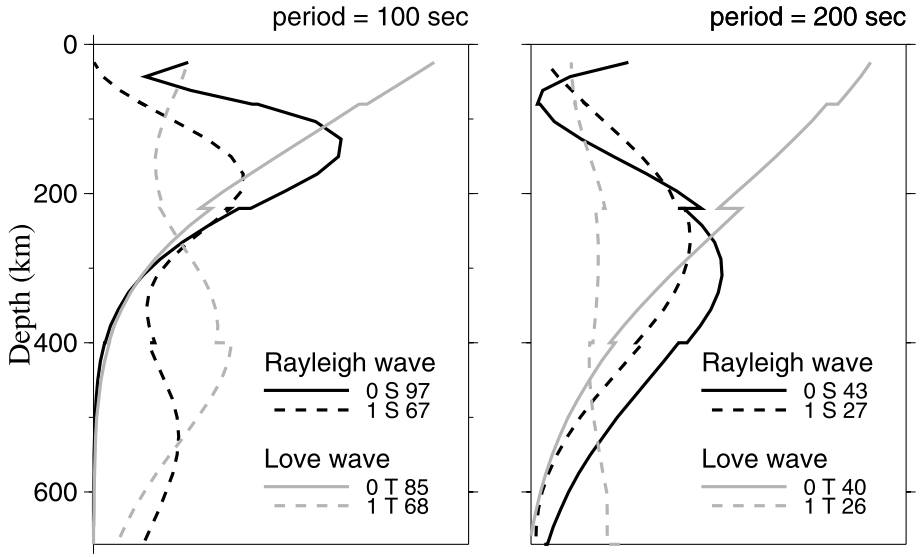

Figure 2. Radial sensitivity kernels to *S* velocity for fundamental mode (solid line) and first overtone (dotted line) Love and Rayleigh wave at periods of 100 and 200 s. Sensitivity kernels to *Q* and to *S* velocity have the same shape.

the resulting model from being biased by the inherent irregular distribution of data coverage, a coverage dependent weighting scheme is applied. For each wave packet, we compute a measure of redundancy with respect to all the other wave packets in the data set. We then assign to the wave packet a weight inversely proportional to the square root of the redundancy estimate. Details of this procedure are given in LR96.

In addition to Rayleigh wave data, a V_{SV} component body wave data set, composed of approximately 38 000 wave packets selected on the vertical and longitudinal components is also used for this whole-mantle parametrized V_{SV} model (Section 4.2).

3 THEORY

Based on asymptotic expressions of Romanowicz (1987) and Li & Tanimoto (1993), LR95 developed the non-linear asymptotic coupling theory (NACT), in which long-period acceleration seismograms can be represented as:

$$u(t) = \sum_k A_k \exp(i\widehat{\omega}_k t) + u_1(t). \tag{1}$$

The first term on the right hand side of eq. (1) is the exact result of conventional path-average approximation (PAVA) (e.g. Woodhouse & Dziewonski 1984; Tanimoto 1986); the second term $u_1(t)$ represents the cross-branch modal coupling effect ignored by the PAVA. As demonstrated in LR95 and Mégnin & Romanowicz (1999), because across-branch coupling provides 2-D kernels appropriate for body waveforms that sample the deep mantle, NACT is significantly more powerful in resolving 3-D structure in the mid and lower mantle. While the NACT sensitivity kernels for deep-sampling body waves are very different from those of PAVA, they are similar for surface waves. Moreover, the dense data coverage in the upper mantle can also reduce the bias caused by horizontal averaging of the PAVA method. The whole-mantle velocity models used in this study are derived using NACT with both body waves and surface waves. On the other hand, only surface waves are analysed for the upper-mantle *Q* structure. For now, we will apply PAVA instead of NACT during the *Q* inversion, i.e. the second term on the right hand side of eq. (1), $u_1(t)$, will be neglected. This represents considerable computational savings. In the future, as we proceed to include body waves, NACT kernels will need to be considered.

In eq. (1), the summation is taken over all the multiplets with $A_k \equiv \sum_m R_k^m S_k^m$ and

$$\widehat{\omega}_k = \omega_k + \delta\widetilde{\omega}_k, \tag{2}$$

where ω_k is the complex eigenfrequency of multiplet k in the reference symmetrical earth model and $\delta\widetilde{\omega}_k$ is the PAVA apparent frequency shift on the minor arc given by:

$$\delta\widetilde{\omega}_k = \frac{1}{\widehat{SR}} \int_S^R \delta\omega^k_{\rm local} d\phi, \tag{3}$$

where the integration is taken along the great circle path between the source *S* and the receiver *R*, $d\phi$ denotes the incremental angular distance element and $\widehat{SR}$ is the total length of the path. $\delta\ \omega^k{}_{\rm local}$ is the local frequency introduced by Jordan (1978) and is given by

$$\delta\omega^k_{\rm local} = \frac{1}{2\omega_k}\left[\int_0^{R_\oplus} \delta\mathbf{m}(r,\theta,\phi)\cdot\mathbf{M}_k(r) r^2\, dr - \sum_d r_d^2 h_d(\theta,\phi) H^d_k\right], \tag{4}$$

where $R_\oplus$ is the radius of the Earth, δ **m** represents the volumetric perturbations to the elastic reference model and h_d is the perturbations in the radius r_d of the dth radial discontinuity in the reference model. The kernels $\mathbf{M}_k(r)$ and $H^d{}_k$ may be evaluated directly using eqs (A36)–(A42) of Woodhouse (1980).

When anelastic dispersion effects are neglected, the complex perturbation in the eigenfrequency can be written in the form (e.g. Dahlen & Tromp 1998)

$$\delta\widetilde{\omega} = \delta\widetilde{\omega}_0 + i\omega_0\delta\frac{1}{2Q}, \tag{5}$$

where the real part, $\delta\widetilde{\omega}_0$, represents the frequency shift with respect to ω_0, the eigenfrequency in the reference elastic model and is related to the elastic variation in Earth structure; $\delta\frac{1}{2Q}$ is the anelastic perturbation with respect to the reference attenuation model.

In this preliminary study, we do not explicitly correct for focusing effects as a result wave propagation in a 3-D elastic model. Although

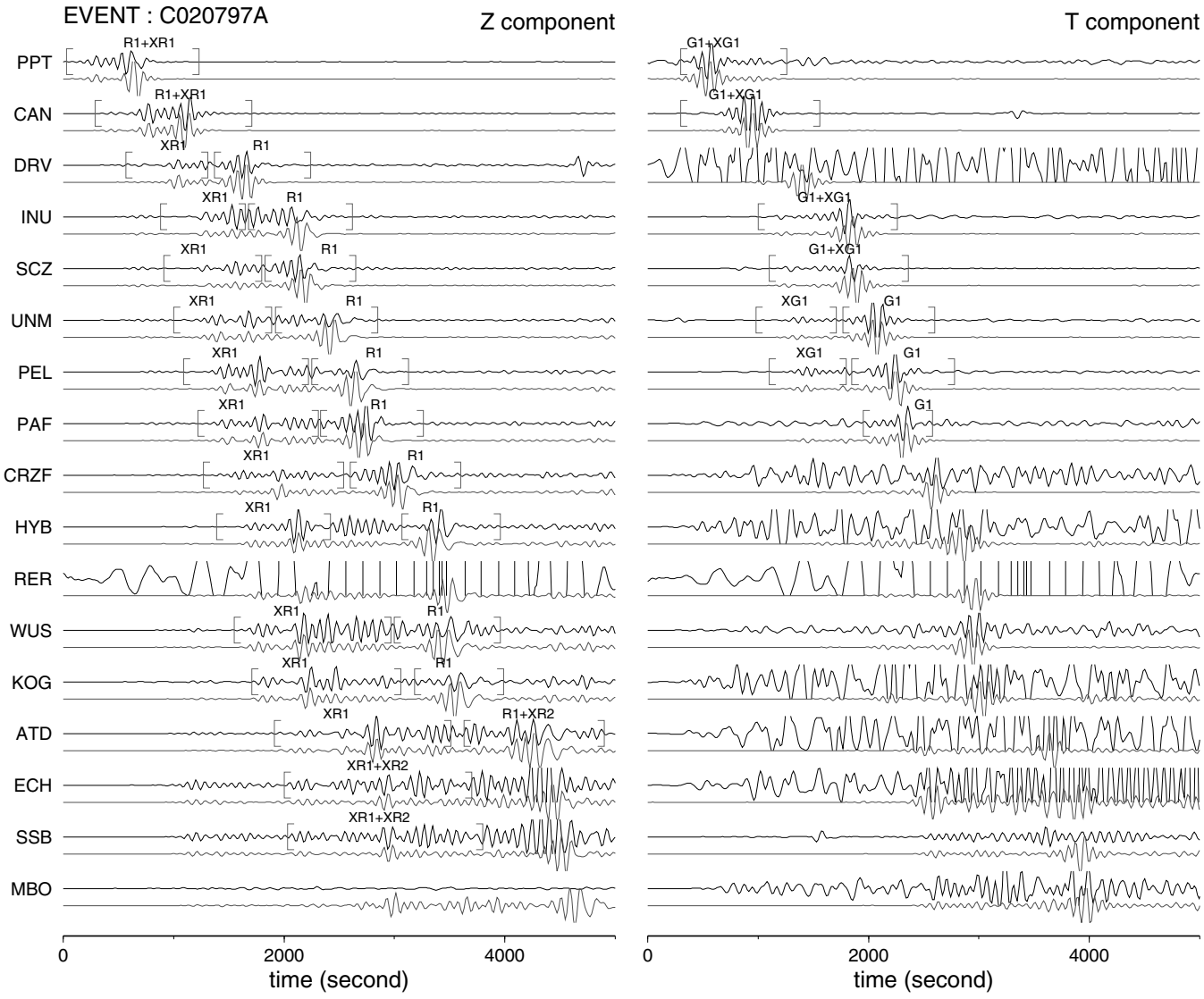

Figure 3. Low-pass filtered ($f < 1/60$ Hz) vertical and transverse component surface wave seismograms for the 1997 February 7 Tonga Islands earthquake recorded at Geoscope stations. The observed seismograms (black) are plotted superimposed on the reference PREM synthetic seismograms with ellipticity included (grey). Only data within the indicated time windows are used in the inversions. The noisy seismograms without time windows have been rejected by the automatic picking algorithm. Note that the horizontal component traces are much noisier than vertical component traces. As a result, fewer wave packets in horizontal component are selected.

these effects can be strong (e.g. Romanowicz 1994), they are dependent on the lateral gradients of the 3-D elastic model, which in turn depend on the short-wavelength features of the elastic model and are not presently well constrained. However, Romanowicz (1995) has demonstrated that the focusing/defocusing effects are small in the retrieved low-degree (*ca* 5–6) Q map. More recently, Selby & Woodhouse (2000, 2002) have also shown that amplitude variations are dominated by intrinsic attenuation at long wavelengths, specifically, for spherical harmonics degrees up to approximately degree 8. To stay within the range where these unmodelled effects are small, we limit our Q model to degree 8 and also perform a careful data selection, as was discussed in the previous section.

Comparison of models obtained using different components of data, bootstrapping tests and examination of the contamination from focusing effects, as will be seen, confirm the stability of the main features of our models.

3.1 Model parametrization

Our velocity and Q models are both parametrized in spherical harmonics for lateral variations and cubic b-splines for depth dependence (e.g. MR00). The velocity model is expressed as perturbations from the spherically symmetric model PREM and is parametrized radially in 16 cubic b-splines for the whole mantle, with the same knot distribution as used in SAW24B16. The Q model is expressed as perturbations from the reference Q model and is parametrized radially in seven cubic b-splines defined from the depth of 80 km to the bottom of the upper mantle (Fig. 5):

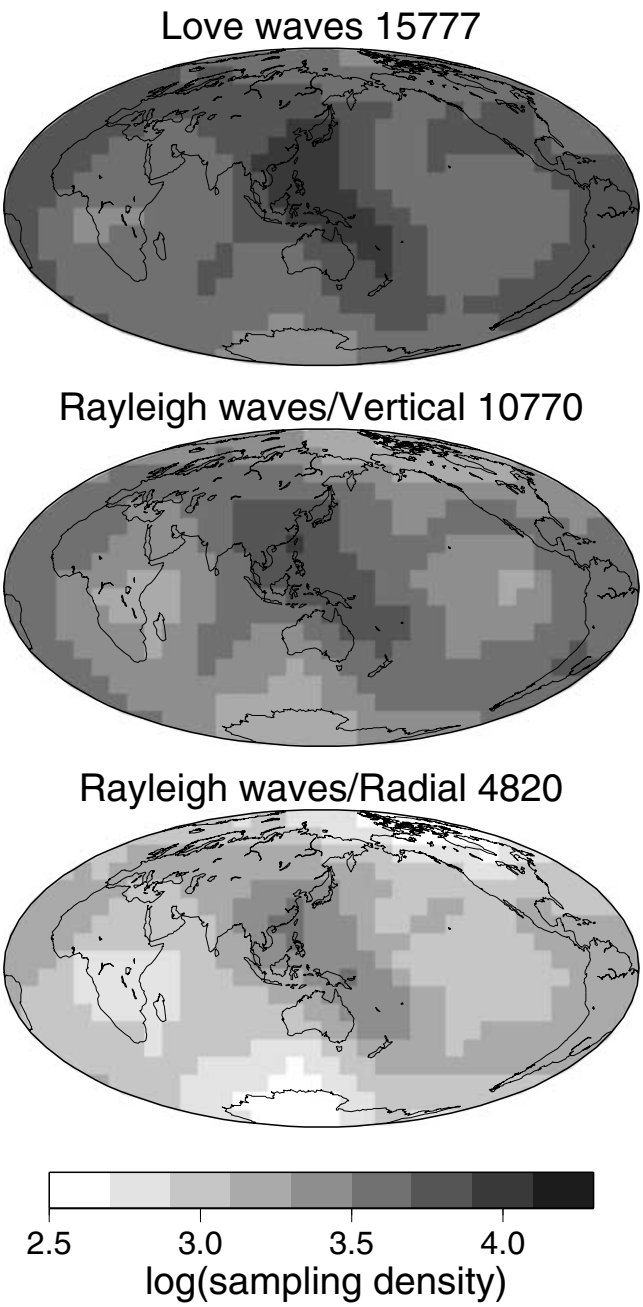

Figure 4. Path density coverage achieved in this study, expressed as the logarithm of the ray length (in degrees) in each 10° by 10° cell, corrected for latitude. The total number of wave packets collected for each component is also shown.

$$\delta \mathbf{m_v}(r,\theta,\phi) = \delta v(r,\theta,\phi)/v_{\mathrm{PREM}}(r) = \sum_{k=1}^{16}\sum_{s=0}^{v_{\mathrm{smax}}}\sum_{t=-s}^{s} {}_k a_s^t B_k(r) Y_s^t(\theta,\phi), \quad (6)$$

$$\delta \mathbf{m_q}(r,\theta,\phi) = \delta q_\mu(r,\theta,\phi) = \sum_{k=1}^{7}\sum_{s=0}^{q_{\mathrm{smax}}}\sum_{t=-s}^{s} {}_k b_s^t B_k(r) Y_s^t(\theta,\phi), \quad (7)$$

where $\delta\ \mathbf{m_v}$ and $\delta\ \mathbf{m_q}$ are the volumetric perturbations in S velocity and attenuation, v_{smax} and q_{smax} are maximum degree in the horizontal spherical harmonics parametrization for velocity and Q models

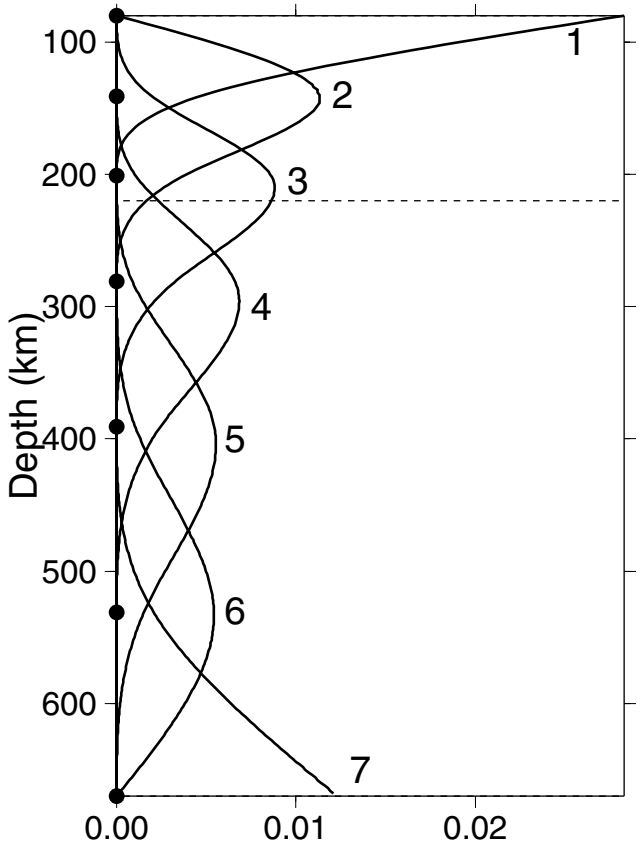

Figure 5. The cubic b-splines used as basis functions, for the radial parametrization used in the Q inversion.

respectively and $B_k(r)$ are cubic b-splines, as defined in MR00. In both models, the knots are distributed with progressively shorter spacing at the shallower depths to reflect the radial resolution of our data. $Y_s^t(\theta,\phi)$ are fully normalized spherical harmonics as defined in Edmonds (1960), $q = Q^{-1}$, and ${}_k a^t{}_s$ and ${}_k b^t{}_s$ are the model coefficients to be determined in the inversion.

The maximum degree of the lateral spherical harmonics expansion is 16 for the SV-velocity model and 8 for the Q model, for the reasons discussed above.

3.2 Inversion

The partial derivatives of a seismogram with respect to model coefficients, ${}_k a^t{}_s$ and ${}_k b^t{}_s$, can be derived from eqs (1–7). The inverse problem is then solved using a stochastic formalism (Tarantola & Valette 1982) and the finite-dimensional model is obtained by the recursive application of a Newton scheme to the Fréchet derivatives of the ℓ^2-norm objective function. We refer the reader to LR96 for the details of the inversion.

The elastic and anelastic model coefficients are solved separately. We first solve for the 3-D elastic model, which is then used to align the phase of data and synthetics prior to the Q inversion. The reason for this sequence of inversions will be given in the next section, which discusses the results of test inversion experiments.

Source parameters are kept fixed as given in the CMT catalogue (Dziewonski *et al.* 1981). We discuss this point in a later section.

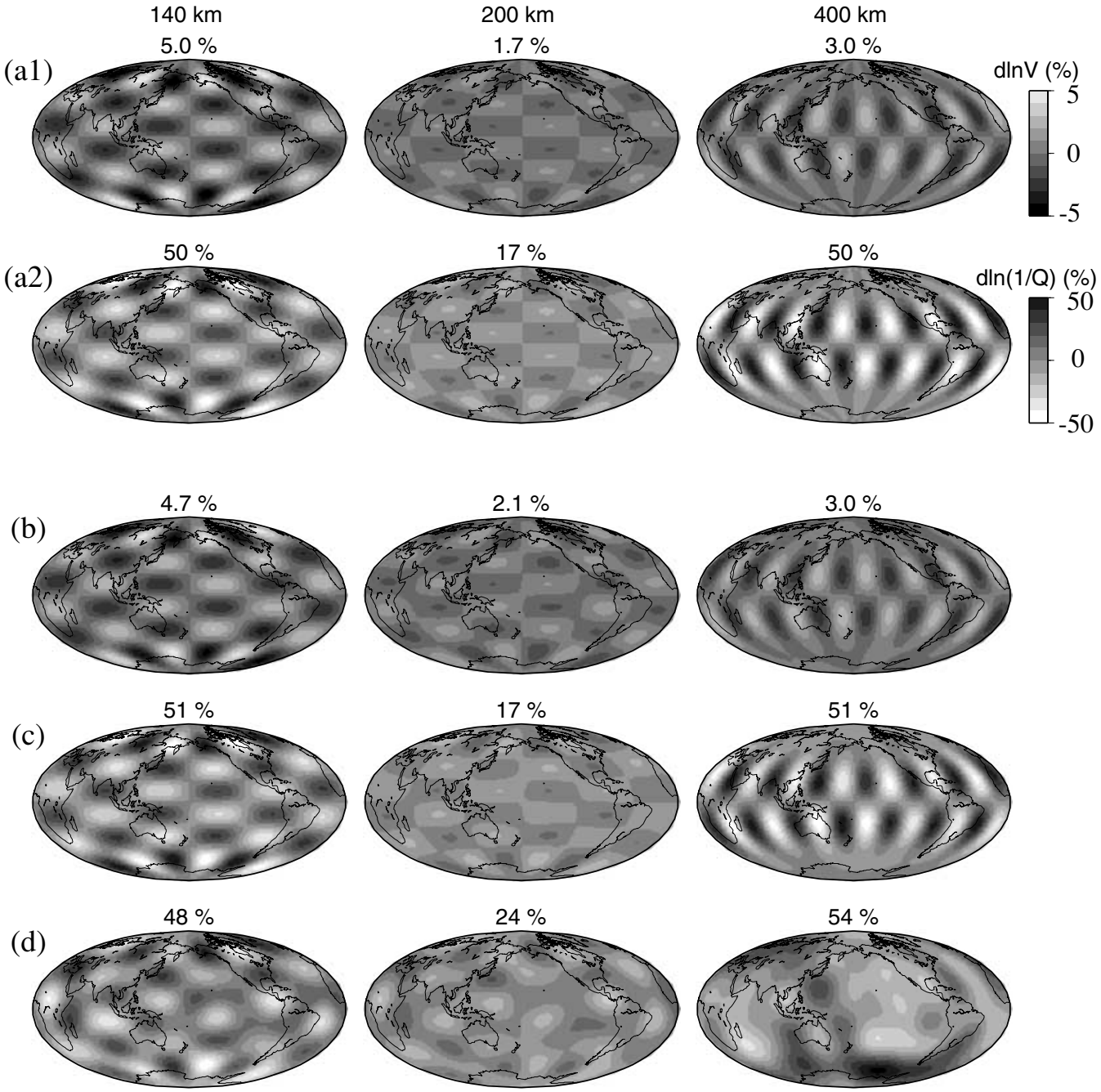

Figure 6. Input models and results of synthetic inversions: (a1) input V_S model; (a2) input Q model; (b) inverted velocity model without accounting for the 3-D Q effects; (c) inverted Q model with phase correction based on the velocity model shown in (b); (d) inverted Q model without 3-D elastic corrections.

4 INVERSION EXPERIMENTS AND INVERSION PROCEDURE

For elastic tomography based on waveform data, the phase deviation between observed data and synthetics is the most useful information, in that the variance reduction is mainly achieved by means of phase alignment. Although attenuation heterogeneities could cause phase distortion in the waveform, their main effect is in the amplitudes. This has the following consequence when using waveform data for elastic and anelastic tomography: whereas amplitude variations as a result of anelastic heterogeneities can be ignored in elastic tomography, the phase shift caused by elastic heterogeneities needs to be considered in anelastic tomography. Indeed, a correct point-by-point matching of amplitudes of synthetic and observed waveforms is impossible when their phases are not well aligned. Also, if the phases are not aligned, because the most efficient way to minimize the variance between data and synthetics is to decrease the amplitudes of synthetics, the derived Q model can be biased.

4.1 Inversion experiments

We implement an inversion experiment to test these assertions and explore the interaction between elastic and anelastic tomography. The procedure and results are as follows:

(i) Generate the predicted radial component of Rayleigh waves from a test input model. The coverage and frequency band of synthetic data are exactly the same as for the data used in this study. The test input model contains two levels of degree-8 heterogeneities both in velocity and attenuation. The heterogeneities are distributed around depths of 150 km (5 per cent for $d \ln V_S$ and 50 per cent for $d \ln Q^{-1}$) and 400 km (3 per cent for $d \ln V_S$ and 50 per cent for $d \ln Q^{-1}$) respectively, as shown in Fig. 6(a). We note that, given these elastic and anelastic variations, we find that the mean variance of synthetic data as a result of Q heterogeneities is only approximately 6.4 per cent of the total variance resulting from both the Q and velocity heterogeneities. Therefore, we do not expect a large variance reduction as a result of Q structure when using real data.

(ii) Invert for a velocity model based on the synthetic data set, without modelling the effects of attenuation heterogeneities. The same inversion technique used for real data is applied. The result (Fig. 6b) shows that both the lateral variations and amplitudes of the input velocity model are well recovered. This confirms that the amplitude variations resulting from anelastic perturbations are not an impediment to elastic waveform tomography.

(iii) Invert for attenuation model. Two experiments are conducted: one with and one without phase correction for velocity heterogeneities. Fig. 6(c) shows that the input Q images at both depths are well recovered, when phase correction is applied prior to the Q inversion (using the retrieved velocity model in the last procedure). When the elastic heterogeneities are ignored, the input Q model, especially its deeper structure, is poorly resolved (Fig. 6d). This result shows that the phase shift correction for the 3-D elastic model is a prerequisite for Q tomography using waveforms.

In the above experiments, the elastic effects in the amplitudes are not modelled. The potential contamination on the resulting Q model from focusing effects will be evaluated in a later section.

4.2 Inversion procedure

Accordingly, the inversion procedure based on real data is set as follows:

(i) Invert for velocity models. Because strong anisotropy in the upper mantle has been observed in many studies (e.g. Montagner & Tanimoto 1990; Ekström & Dziewonski 1998), we perform separate inversions of V_{SH} (transverse component) and V_{SV} (vertical and longitudinal component) data to better account for the elastic effects in the following Q inversion. For the elastic inversions, we consider a data set comprising both surface waves and body waves and we invert for whole-mantle structure using NACT kernels. We already have a satisfactory V_{SH} elastic model, SAW24B16. Starting from SAW24B16, truncated to degree 16 (the variations beyond degree 16 are essentially insignificant, as long as we ignore the focusing effects), we invert for a degree-16 V_{SV} model. Before the inversion, the crustal effects are corrected for by using the global crustal model, CRUST 5.1 (Mooney *et al.* 1998).

(ii) Invert for a degree-8 Q model using three-component waveforms simultaneously. To prevent the Q model from being biased by unmodelled elastic effects in the phases, waveform correlation is used as a data selection criterion before Q inversion, as described in Section 2. To further emphasize the contribution of data whose phase is well aligned, an additional weighting factor proportional to the waveform correlation is assigned to each wave packet during the Q inversion. Each data set (vertical, longitudinal and transverse components) is weighted such that the weighting of Love waves and Rayleigh waves is balanced on the one hand and, on the other hand, so is the weighting of vertical and radial component of Rayleigh waves. The V_{SH} model is used for the phase corrections on Love wave data and the V_{SV} model on Rayleigh wave data.

Inversion for Q is limited to the depth range 80–670 km, because resolution is poor at shallower depths. Moreover, because Q in the crust is very large, sensitivity of long-period surface wave data to lateral variation of Q in the crust is relatively small, even though there are significant lateral variations of Q in the crust(e.g. Mitchell 1995).

Regarding crustal corrections, we consider the radially symmetric model QL6 and replaced its flat Moho by undulations, according to model CRUST 5.1, to account for the distinct Q values across the Moho (e.g. PREM, QL6).

5 RESULTS

In what follows, we present our results both for velocity models and Q models, and then discuss the results of various experiments performed to test the stability of the Q models. The discussion of velocity models will be brief, because the Q model is the focus of this paper.

5.1 Velocity models

In Fig. 7, we show maps of V_{SV}/SAW16BV and V_{SH}/SAW24B16 models at several depths in the upper mantle. In general, the main features in these two models are similar. The main difference is in the central Pacific at a depth range around 200 km, where opposite variations of V_{SH} (faster than average) and V_{SV} (slower than average) are observed. Besides this well documented anisotropic feature (e.g. Montagner & Tanimoto 1990; Ekström & Dziewonski 1998), some other interesting features are also observed in the comparison between V_{SH} model and V_{SV} model. For example, a faster than average signature of continental roots in the V_{SV} model fades off at a shallower depth (*ca* 200–250 km) compared with that in the V_{SH} model (*ca* 350–400 km). These features have been confirmed by performing a joint anisotropic inversion on three-component waveform data, in which the effects of V_{SV} on toroidal modes and V_{SH} on spheroidal modes are also incorporated. We refer the reader to Gung *et al.* (2003) for detailed discussion on the tectonic corresponding implications.

5.2 3-D Q model

Three different 1-D Q models have been tested as starting models (Fig. 8). These include QL6, QR19 (degree-0 term) and QL6c (a smoothed version of QL6). Although the inverted Q models show similar patterns, those from smooth 1-D Q models are more stable across the 220 km discontinuity because the smooth parametrization is more compatible with the spline parametrization in the depth of the 3-D Q model. For simplicity, we will only display the results derived from QL6c. Because we do not adjust the seismic moment, which trades off with radial Q structure, we do not present or discuss the degree-0 term of our Q models.

Maps of the 3-D Q model derived using three-component data, QRLW8, are presented in Fig. 9. The lateral variations are expressed in terms of relative variations in Q^{-1} with respect to QL6c. The blue and red colors correspond to high Q (low attenuation) and low Q (high attenuation), respectively. The surface positions of hotspots,

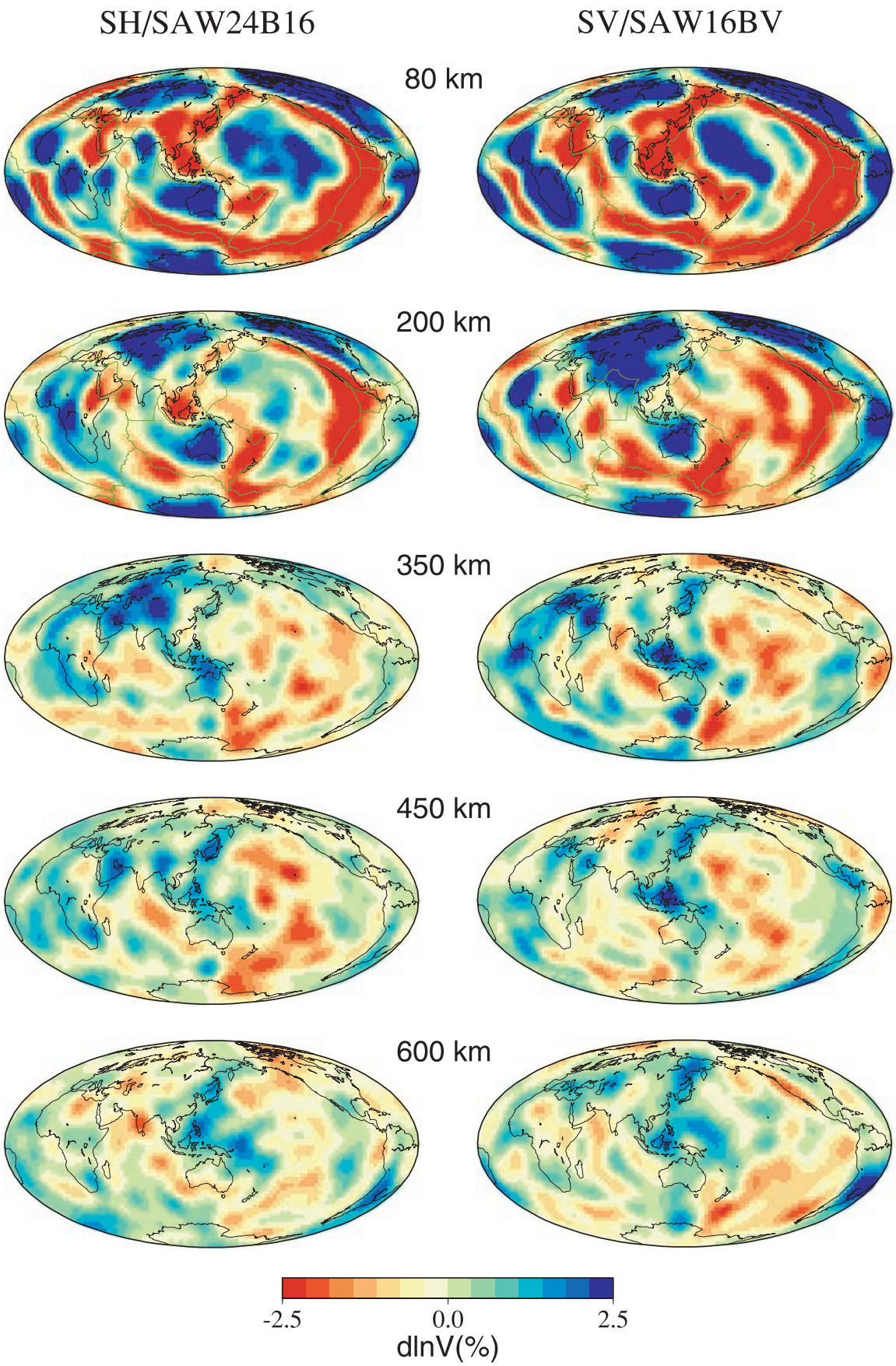

Figure 7. Comparison of V_{SH} (SAW24B16) and V_{SV} (SAW16BV) models. The degree-24 SAW24B16 model is truncated to degree 16.

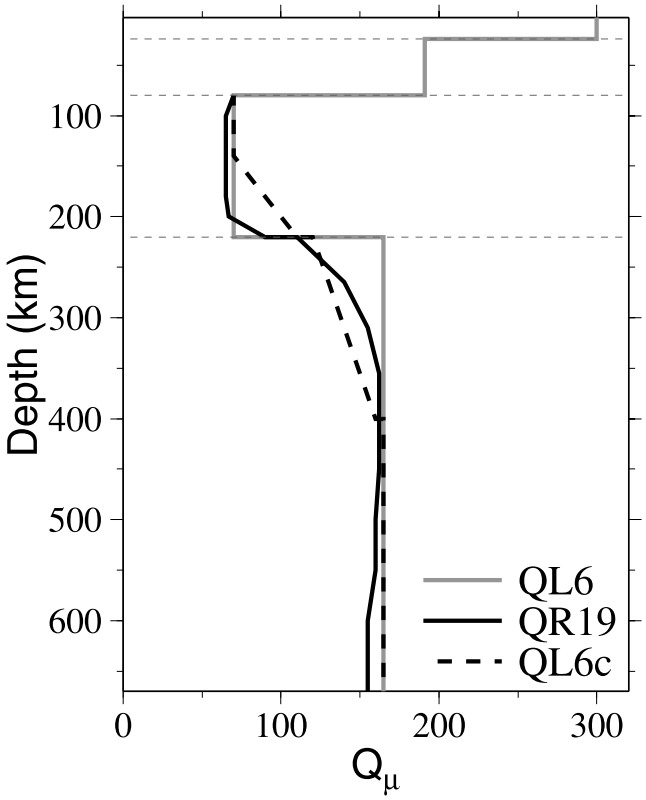

Figure 8. Three starting 1-D Q models used in the Q inversion, QL6 (Durek & Ekström 1996), QL6c and degree-0 term of QR19 (Romanowicz 1995). QL6c is modified from QL6 by smoothing across the 220 km discontinuity.

according to the list by Richards *et al.* (1988) are also shown as black dots in the maps at depths greater than 300 km.

In the depth range above 200 km, we find a good correlation between the distribution of Q and tectonics. The lowest Q anomalies are located under the East Pacific rise, Mid-Atlantic ridge, Indian ridges, backarc regions of the western Pacific, and in the Mediterranean. Such low-Q features under ridges and backarcs have also been documented in other regional Q studies (e.g. Ding & Grand 1993; Flanagan & Wiens 1994; Roth & Wiens 1999). We also note a low-Q zone centered in the southern Pacific extending north to Hawaii. This low-Q zone (which does not have an obvious correspondence in elastic velocity models at shallow depths) becomes stronger with depth and is one of the two most prominent low-Q anomalies at depths below 200 km.

At depths shallower than 200 km, high-Q anomalies are generally found in tectonically stable areas, such as the Canadian shield, Australia, Siberia, Antarctica, the Russian platform, Brazil and Africa.

This tectonic-related Q distribution at shallow depths is consistent with other global Q models obtained using various data and techniques (e.g. Bhattacharyya *et al.* 1996; Selby & Woodhouse 2000; Reid *et al.* 2001; Selby & Woodhouse 2002; Warren & Shearer 2002). In Fig. 10, we compare the average Q structure in the depth range 80–200 km with two other recent global Q models: the Q_α model presented by Warren & Shearer (2002) (a 2-D model of the top 220 km of the mantle) and the degree-20 Q_μ model by Selby & Woodhouse (2000), which is constructed from Rayleigh waves. Here we show its Q_μ map at the period of 73 s. Even though they are derived from different approaches, the tectonic-related Q distribution in the shallow mantle is present in all these models. One significant difference among the three models lies under the south central Pacific, where the low Q anomaly is not observed in the other two models. The low-Q anomaly shown in QRLW8 extends from the top of our model to the transition zone, where it is somewhat shifted towards the south. We discuss the possible source of this anomaly in Romanowicz & Gung (2002) as related to horizontal flow of heat (and possibly matter) in the asthenosphere, connecting the superplume center in the south Pacific to Hawaii. This is consistent with the strong transverse isotropy observed in the central Pacific with $V_{SH} > V_{SV}$, as discussed in Romanowicz & Gung (2002). Our study includes constraints from the analysis of Love wave data, which have strong sensitivity to shallower depths. Such constraints are not included in the study of Selby & Woodhouse (2002), while bounce *PP* bounce points may not be dense enough in the study of Warren & Shearer (2002) to resolve this feature.

Between 200 and 300 km, the tectonic-related Q distribution in QRLW8 is gradually replaced by a simpler pattern. The strongest low-Q anomalies are under the central Pacific, the south Atlantic and southern Africa. Some strong low-Q anomalies at shallow depths disappear, such as the most notable low-Q features below the East Pacific rise, Atlantic ridge, India ridge and western Pacific backarcs. The observation of shallow roots of low Q beneath mid-ocean ridges supports the passive character of the ridge system and is in agreement with velocity models, where the low-velocity signature of oceanic ridges is also largely limited to the topmost mantle (e.g. Zhang & Tanimoto 1993). Similarly, some shield-related high-Q regions also taper off within this depth range, such as southern Africa, Antarctica and part of America.

At depths greater than 400 km, the Q distribution is generally dominated by two strong minima, one under the southern Pacific and one under Africa, yielding a strong degree-2 pattern. We also find that a majority of hotspots are located above regions of low Q, which is consistent with QR19, in which a tectonic-correlated Q distribution at shallow depths is gradually replaced by a hotspot-correlated pattern at larger depths. The degree-2 pattern of attenuation in the upper-mantle transition zone was also found in previous studies (e.g. Romanowicz *et al.* 1987; Roult *et al.* 1990; Suda *et al.* 1991) using complex frequency measurements of fundamental spheroidal modes. In the degree-2 pattern of QRLW8, the two low-Q minima are, strikingly, positioned above the two superplumes documented in the lowermost mantle from elastic tomography [e.g. LR96; Masters *et al.* (1996); MR00; Gu *et al.* (2001)], which themselves have been shown to be well correlated with the degree-2 geoid as well as with the hotspot distribution (e.g. Richards *et al.* 1988).

This correlation and its geodynamic implications have been discussed in Romanowicz & Gung (2002). We will now discuss the stability of the Q model.

5.3 Discussion of model stability

5.3.1 Q models from different data sets

In Fig. 11, we present the Q models inverted separately from the transverse component (QL), radial component (QRr) and vertical component (QRv). The depth correlation between QRr and QRv is also shown. The QL model is shown only at shallow depth, as Love waves have limited resolution at larger depths. Although the models differ in some details, similar Q distributions are observed at shallow depth (180 km) in all models, with low attenuation under continents and high attenuation under ridges and backarcs. The low-Q region in the central Pacific is stronger and extends further north in the transverse component (Love wave) model. This may be an

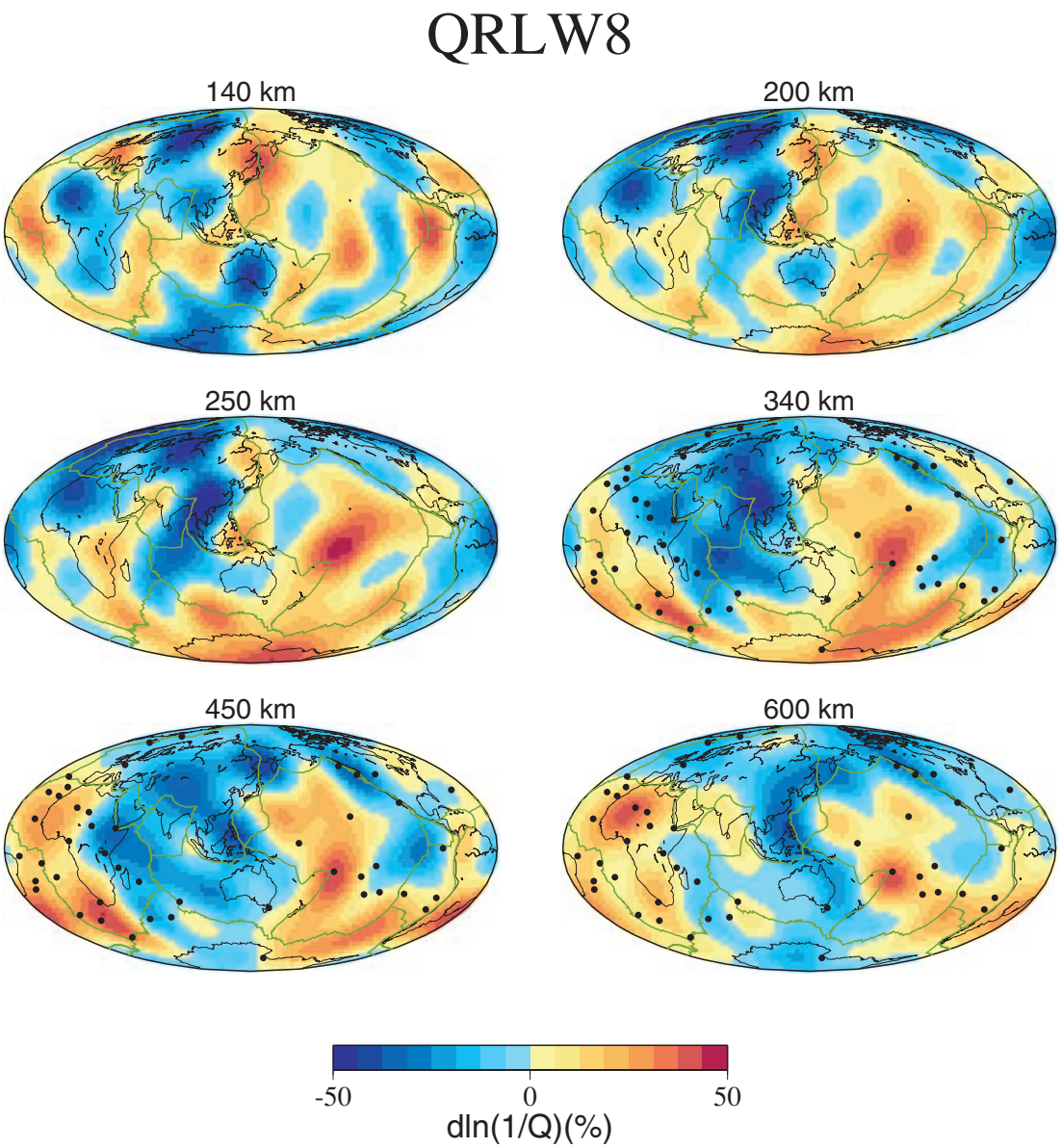

Figure 9. Model QRLW8 derived from three-component data. Black dots are hotspots according to the list by Richards *et al.* (1988).

indication of anisotropy in Q, however, we do not feel we are able to resolve this confidently. The QRr and QRv models are also in good correspondence at greater depth, showing low-Q regions under Africa and the Pacific. The depth correlation between QRr and QRv is larger than 0.6 at all depths, in spite of their different data coverage. Indeed, fewer radial component traces are available as a result of the more noisy character of horizontal component data. While it is interesting to note the relatively good agreement between the different models, combining three-component data to obtain model QRLW8 results in better depth resolution and more robust features.

5.3.2 Resolution analysis

We implement resolution tests to further inspect the robustness of the pattern obtained in the upper-mantle transition zone. Unlike the commonly used checkerboard model, we construct a test input model by setting two opposite degree-2 patterns in the top two splines corresponding to the shallow parts of the depth parametrization, which cover the uppermost mantle (80 to *ca* 200 km) and in the fifth and the sixth splines, which cover the transition zone (*ca* 300 to *ca* 600 km). The resolution matrix (e.g. Aki & Richards 1980; LR96) is directly obtained from the combination of partial derivative matrix and model covariance matrix used for the inversion with real three-component data. The result is shown in Fig. 12(a). Compared with the uppermost mantle, the transition zone is apparently overdamped as a result of the weaker sensitivity in this depth range combined with unmodelled higher order elastic effects. Nevertheless, the pattern of lateral variations in Q is well recovered and not affected by the opposite pattern in the uppermost mantle. This indicates that the strong degree-2 pattern in the transition zone cannot be an artefact resulting from the leakage of structure in the uppermost mantle. The same experiments are performed at higher degrees. Similarly, the amplitude is well recovered at shallow depth and decreases more at transition zone depths for higher degrees, but the pattern of lateral variations is recovered in both depth ranges. Fig. 12(b) shows the

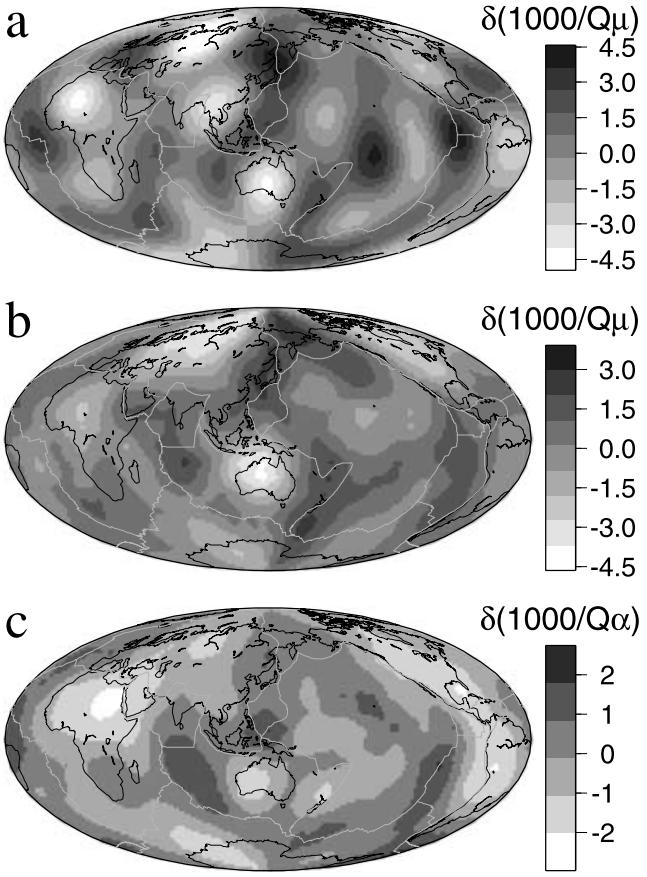

Figure 10. Comparison of Q models: (a)average Q map for the depth range 80–200km of QRLW8, (b)Q_μ model for 73 s Rayleigh waves by Selby & Woodhouse (2000) and (c) Q_α model by Warren & Shearer (2002).

result of a degree-6 resolution test, showing that the same conclusions hold at shorter wavelengths.

Resolution matrix for each single spline, i.e. a subset of the complete resolution matrix, is analysed to further explore the depth dependence of the model resolution. Fig. 13 shows the resolution matrices for the second, fourth and sixth splines. The matrix elements are ordered such that lower degree model coefficients are in the upper-left corner and the higher degree model coefficients are in the lower-right corner of the matrix. The power for the diagonal and off-diagonal elements of the matrix are also shown in the figure. This figure illustrates that (i) the off-diagonal terms are relatively small, (ii) the resolution at shallower depth is better than that at larger depth and (iii) the higher degree coefficients are not well resolved at larger depth. It is also interesting to see that the even degree structure is better constrained than the odd degrees, a characteristic of PAVA as noted by Woodhouse & Dziewonski (1984).

5.3.3 *Bootstrap test*

We apply the bootstrap method to estimate model uncertainties. First, all the data are divided into 12 groups according to their month of recording. Next, 10 groups are successively picked out of 12 to generate a data subset for each test. With all the combinations thus obtained, we construct a data population of 66 data subsets with each subset comprises approximately 83 per cent of the complete data set. The same inversion procedure and damping scheme as used for model QRLW8 are applied to each subset. Finally, the standard deviation of the resulting 66 Q models is used to estimate the uncertainty of the model. In Fig. 14 we show the estimated uncertainties at 200 and 500 km. The maximum amplitude of uncertainty is less than 10 per cent and the uncertainties are less than 5 per cent in most regions. Poor-coverage areas tend to have larger uncertainty, such as the north Pacific and the area between Antarctica and Australia. Also note that the uncertainty is very small in the central Pacific, where the prominent low-Q zone was found.

5.3.4 *Amplitude of lateral variations in Q*

The results of the bootstrap tests are only valid inasmuch as the damping chosen for the inversion is valid. As mentioned previously on the occasion of synthetic tests, the variance in the waveforms is dominated by the phase alignment, therefore, it is mainly contributed by 3-D elastic structure. Thus, it is not surprising that the variance reduction obtained with QRLW8 is only in the order of 7 per cent. On the other hand, the maximum amplitude of the lateral variations in Q varies with the damping chosen in the inversion. Because the Q signal is faint and we do not correct for focusing explicitly, strong damping is necessary to obtain a stable model. We feel that these amplitudes are therefore not well constrained. We conservatively chose a damping scheme that results in amplitudes of approximately 55 per cent at 200 km, but these could be larger by a factor of 2. The corresponding lateral variations in temperature are in the order of 200–400 $^\circ C$, depending on the model chosen for frequency dependence in Q (Karato 1998).

5.3.5 *Assessing the focusing effects*

Although previous studies (Romanowicz 1994; Selby & Woodhouse 2000, 2002) have shown that the focusing/defocusing contamination is not significant in the retrieved long wavelength Q structure, it is important to examine the focusing/defocusing effects with the data set and 3-D elastic model used in this study.

To investigate this, we generate synthetic data by applying higher order asymptotic theory (e.g. Romanowicz 1987; Romanowicz *et al.* 2004), in which the normal mode amplitudes, to order $1/l$, can be expressed as:

$$A_k = A_k^0(1 + \delta F_k), \tag{8}$$

where $A^0{}_k$ is the zeroth order amplitude, as used in path average approximation, and δF_k is the amplitude perturbation term, which depends on the relative strength of great circle and minor arc averages of the local frequency and its transverse first and second derivatives.

Similar to our earlier inversion experiment, data from the radial component of Rayleigh waves with realistic coverage are considered. The phase and amplitude perturbations of synthetics are computed based on our degree-16 SV-velocity model, SAW16BV. No 3-D Q model is used in the generation of synthetics: we assume no lateral heterogeneity in Q.

We then invert for a 3-D attenuation model with the synthetic data, using the same approach as for real data, i.e. correcting for the phase shift and ignoring the elastic amplitude perturbation term. The same damping scheme as used for real data is applied during the inversion. The resulting ghost Q model and its depth correlation to Q model derived from realistic radial component Rayleigh wave data, QRr, are shown in Fig. 15.

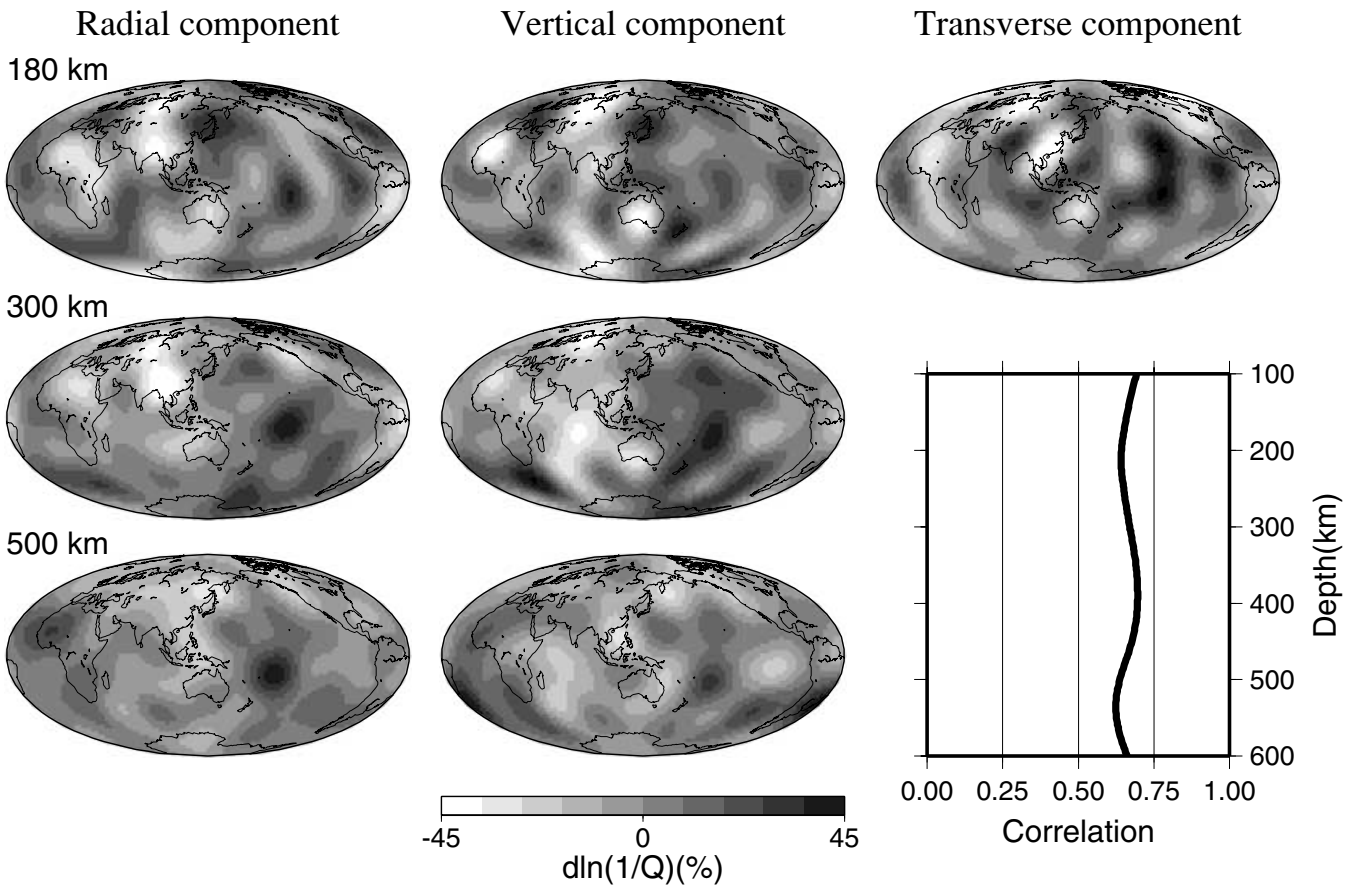

Figure 11. Comparison of Q models derived from different component data [radial (left), vertical (middle) and transverse(right)]. The right panel shows the depth correlation of Q models derived from radial and vertical components.

The low amplitude(< 10 per cent) of the ghost Q model shows that the contamination from uncorrected focusing/defocusing effects is small, in agreement with previous studies (Romanowicz 1994; Selby & Woodhouse 2000, 2002). In particular, its poor correlation (within the range of ± 0.2 at all depths) to QRr demonstrates that our Q model is not strongly biased by the uncorrected focusing/defocusing effects.

With the three-component data used in the derivation of QRLW8, we have also inverted for a tentative degree-8 Q model with focusing effects corrected using SAW24B16 and SAW16BV for Love waves and Rayleigh waves, respectively. The resulting model is shown in Fig. 16, which shows the main features observed in model QRLW8 are stable by the correlation of Q with tectonics at shallow depths and strong degree-2 pattern in the transition zone. This is consistent with the previous experiment indicating that focusing/defocusing effects do not strongly affect the resulting degree-8 Q model.

As mentioned by Romanowicz (1998), our ability to further constrain Q models quantitatively relies strongly on how successful we will be in modelling the effects of elastic structure on seismic wave amplitudes.

The focusing/defocusing of seismic wave amplitudes depends on the higher degree elastic heterogeneities, therefore, robust fine structures in elastic models are required to accurately account for amplitude effects as a result of 3-D elastic structure. This is still a challenge, as current elastic 3-D models differ significantly in their fine scale details.

5.3.6 Source parameters

In this study, we assume that source parameters are as given in the CMT catalogue. Uncertainties in the source parameters could directly affect the inverted Q images. Because our waveform approach does not exclude the effects of source uncertainties, an implicit assumption is that the uncertainties in sources are randomly distributed and the steady signals of the Q structure on the waveforms are not significantly distorted by the random noise of source uncertainties, given a large amount of data.

To assess the effects of source uncertainties on Q tomography, we have performed the following experiments, in which we randomly perturb the six moment tensor parameters of the events in our data set, starting from the CMT solutions. Four ranges of perturbation amplitudes are applied, -5 to 5, -10 to 10, -20 to 20 and -40 to 40 per cent, respectively. The correlation between the resulting Q models and QRLW8 are shown in Fig. 17. The resulting Q images are stable and the correlation to QRLW8 is larger than 0.9 at all depths for Q models with perturbation amplitudes less than 20 per cent. The correlation is larger than 0.7 at all depths even when the perturbation amplitude is as large as 40 per cent.

A similar experiment is implemented to explore the effects from uncertainties in source depth. Three different perturbation amplitudes are applied to events based on their source depths reported in the CMT catalogue. A perturbation amplitude of 10 km is used for events shallower than 30 km, 15 km for events in the depth

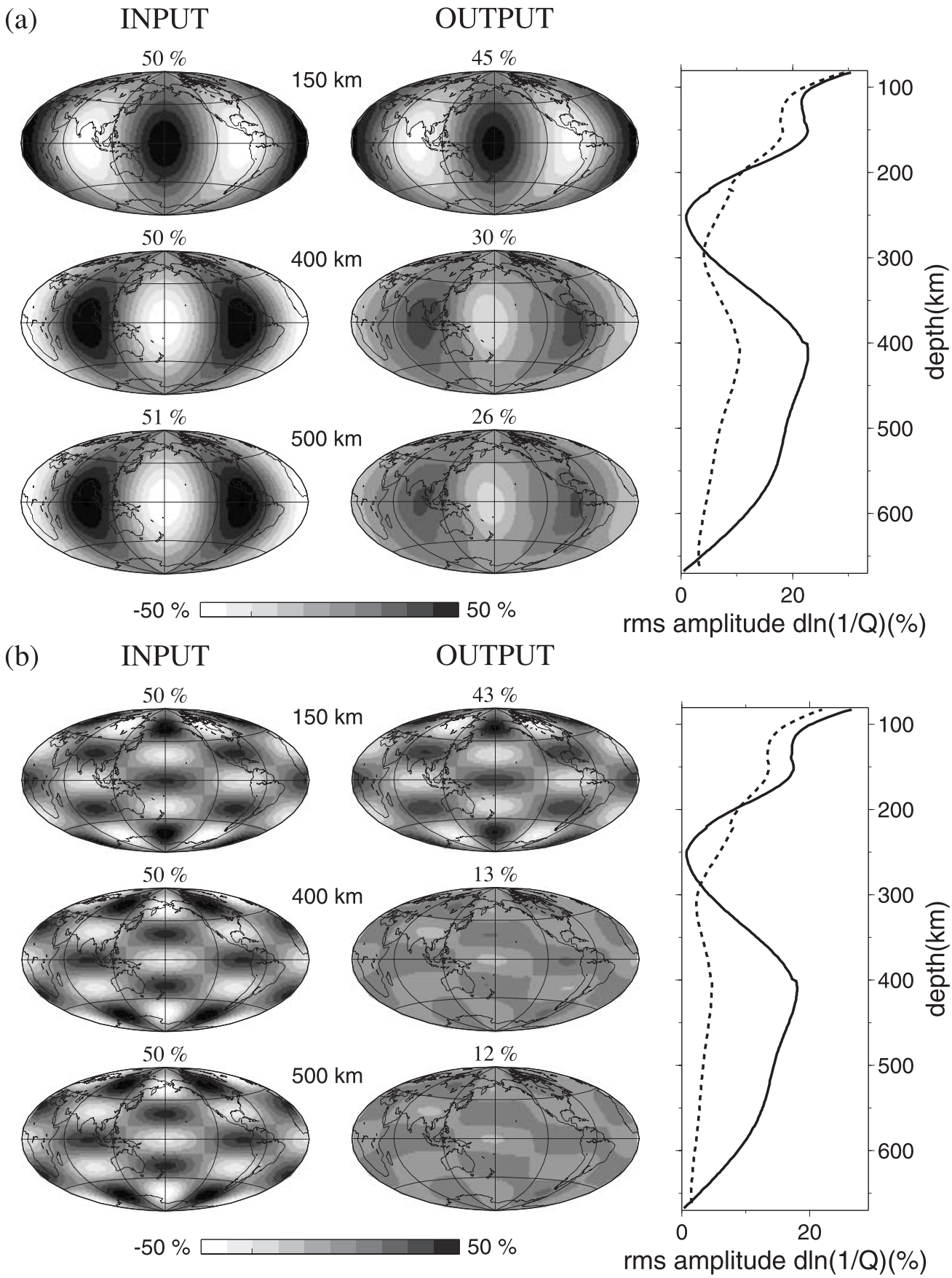

Figure 12. Results of resolution tests: (a) Degree-2 input model (left column) and output model (middle column). The rms amplitude profiles are shown in the right panel, with a solid line for the input model and a dotted line for the output model. (b) Same as (a) for a degree-6 input model.

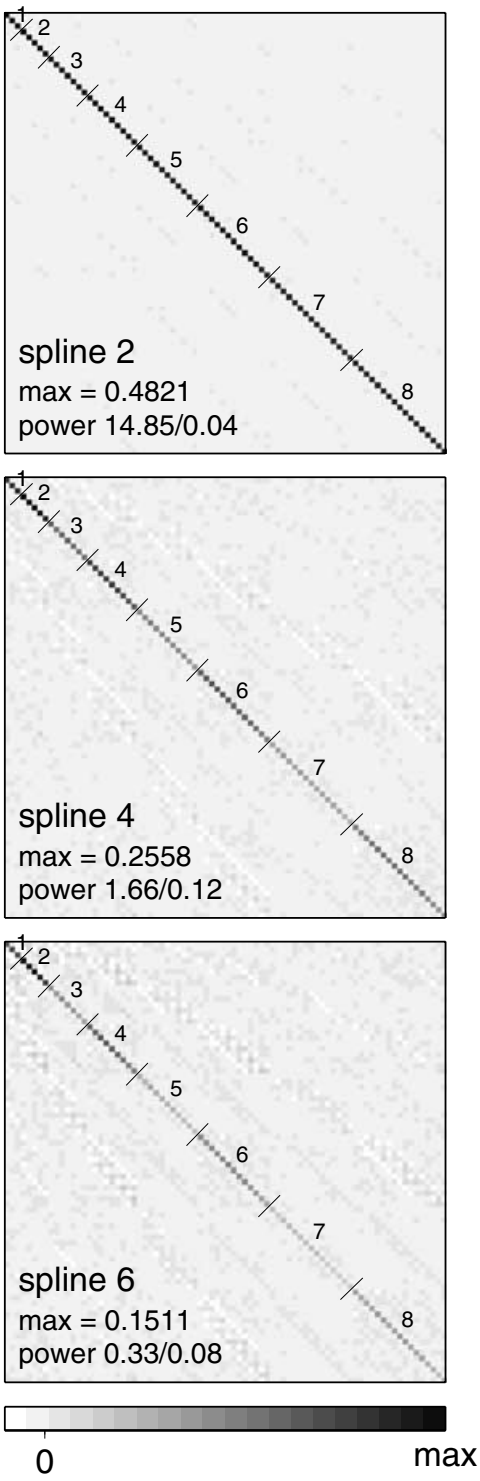

Figure 13. Resolution matrices for for the second (top), fourth (middle) and sixth splines (bottom). Each matrix contains 6400 elements corresponding to the number of model coefficients from degree-1 to degree-8. The matrix elements are ordered such that lower degree model coefficients are in the upper-left corner and the higher degree model coefficients are in the lower-right corner of the matrix. The associated degrees of spherical harmonics are also numbered in each matrix. The maximum values, the powers of the diagonal and off-diagonal elements of each matrix are also shown. For example, the maximum value of matrix elements in the top panel is 0.4821 and the powers for the diagonal and off-diagonal elements are 14.85 and 0.04, respectively.

range from 30 to 100 km and 30 km for events deeper than 100 km. The correlation between the resulting *Q* model and QRLW8 is also shown in Fig. 17. In general, it shows that the above uncertainties in source depth introduces similar effects (in terms of correlation) to those caused by 20 per cent perturbation in amplitude in moment tensors.

Such assumed perturbations are rather large compared with the expected uncertainties in real data, therefore it is clear that uncertainties in source parameters do not influence the main features of QRLW8.

6 CONCLUSIONS

We have presented a 3-D *Q* model of the upper mantle, which has been derived using waveform data of three-component surface waves. The results of this study may be summarized as follow.

(i) *Q* tomography waveform-based inversion is feasible, if appropriate phase corrections based on a 3-D elastic model and careful data selection are applied prior to *Q* inversion.

(ii) Our three-component derived *Q* model, QRLW8, can be divided into two depth ranges. The *Q* distribution above 250 km is generally tectonic-related, which is similar to that observed in elastic velocity models, with regions of high/low velocity correlated to regions of high/low *Q*. A notable exception is an elongated zone of low *Q* in the central Pacific, extending from the south of the equator to Hawaii. This feature is discussed in Romanowicz & Gung (2002), where it is interpreted as the horizontal deflection of plume-related upwelling underneath the lithosphere, and is consistent with the strong transverse anisotropy with $V_{SH} > V_{SV}$ observed under central Pacific (e.g. Montagner & Tanimoto 1990; Ekström & Dziewonski 1998; Gung *et al.* 2003).

Below 250 km, the tectonic-related pattern is gradually replaced by a pattern well correlated with the V_S-velocity distribution in the lowermost mantle, with two strong low-*Q* minima centered in the southern Pacific and under Africa. Most surface hotspot positions are above the low-*Q* areas in the upper-mantle transition zone. We refer the reader to Romanowicz & Gung (2002) for a detailed discussion.

The lateral resolution in our current *Q* model is limited and the amplitudes are not well resolved. Our next steps are: (i) improving the 3-D velocity models by taking into account the anisotropy and focusing effects in the elastic tomography; and (ii) extending this waveform modelling approach to include more realistic focusing effects in the anelastic tomography and source readjustment, based on higher resolution 3-D velocity models.

ACKNOWLEDGMENTS

The authors thank Jeannot Trampert and Anatoii Levshin for helping to improve this manuscript. The authors also wish to thank the IRIS and GEOSCOPE projects for providing the data. This material is based upon work partially supported by the National Science Foundation under Grant Nos EAR-0001965 and EAR-0112409. This is Berkeley Seismological Laboratory contribution no. 04-02.

REFERENCES

Aki, K. & Richards, P.G., 1980. *Quantitative Seismology: Theory and Methods,* W. H. Freeman, New York.

Bhattacharyya, J., Master, G. & Shearer, P., 1996. Global lateral variations of shear wave attenuation in the upper mantle, *J. geophys. Res.,* **101,** 22 273–22 289.

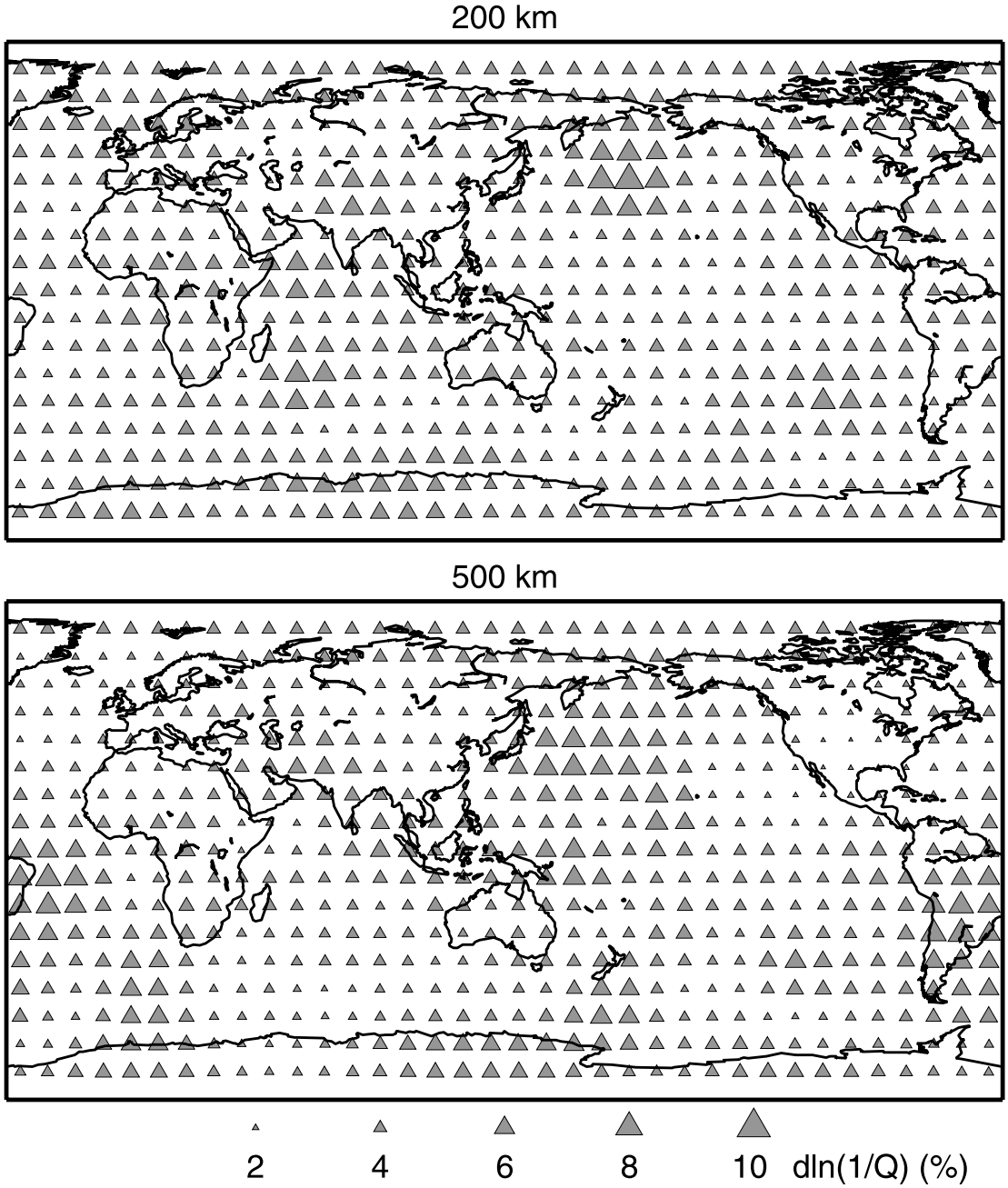

Figure 14. Error estimates at depths of 200 and 500 km from the bootstrap test.

Billien, M., Lévêque, J.-J. & Trampert, J., 2000. Global maps of Rayleigh wave attenuation for periods between 40 and 150 seconds, *Geophys. Res. Lett.,* **27,** 3619–3622.

Dahlen, F.A. & Tromp, J., 1998. *Theoretical global Seismology,* Princeton University Press, Princeton, NJ, p. 1025.

Ding, X.Y. & Grand, S.P., 1993. Upper mantle Q structure beneath the east pacific rise, *J. geophys. Res.,* **98,** 1973–1985.

Durek, J.J. & Ekström, G., 1996. A radial model of anelasticity consistent with long period surface wave attenuation, *Bull. seism. Soc. Am.,* **86,** 144–158.

Durek, J.J., Ritzwoller, M.H. & Woodhouse, J.H., 1993. Constraining upper mantle anelasticity using surface amplitudes, *Geophys. J. Int.,* **114,** 249–272.

Dziewonski, A.M. & Anderson, D.L., 1981. Preliminary reference Earth model, *Phys. Earth planet. Int.,* **25,** 297–356.

Dziewonski, A.M., Chou, G. & Woodhouse, J.H., 1981. Determination of earthquake source parameters from waveform modeling, *J. geophys. Res.,* **86,** 2825–2852.

Edmonds, A.R., 1960. *Angular momentum in quantum mechanics*, Princeton University Press, Princeton, NJ.

Ekström, G. & Dziewonski, A.M., 1998. The unique anisotropy of the Pacific upper mantle, *Nature* **394,** 168–171.

Flanagan, M.P. & Wiens, D.A., 1994. Radial upper mantle attenuation structure of inactive back arc basins from differential shear wave measurements, *J. geophys. Res.,* **99,** 15 469–15 495.

Grand, S., van der Hilst, R.D. & Widiyantoro, S., 1997. Global seismic tomography: a snapshot of convection in the Earth, *GSA Today,* **7**(4), 1–7.

Gu, Y.J., Dziewonski, A.M., Su, W.-J. & Ekström, G., 2001. Models of the mantle shear velocity and discontinuities in the pattern of lateral heterogeneities, *J. geophys. Res.,* **106,** 11 169–11 200.

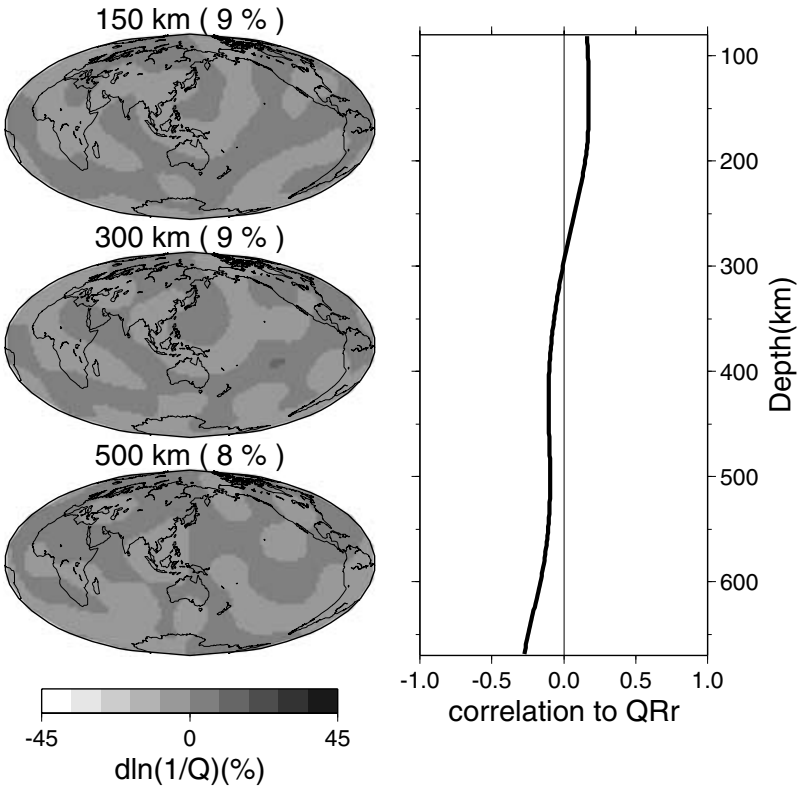

Figure 15. Results of synthetic experiment on focusing/defocusing effects: ghost *Q* model projected from uncorrected focusing/defocusing effects in 3-D elastic model, SAW16BV (left); the depth correlation between ghost *Q* model and QRr (right; please see text for the details).

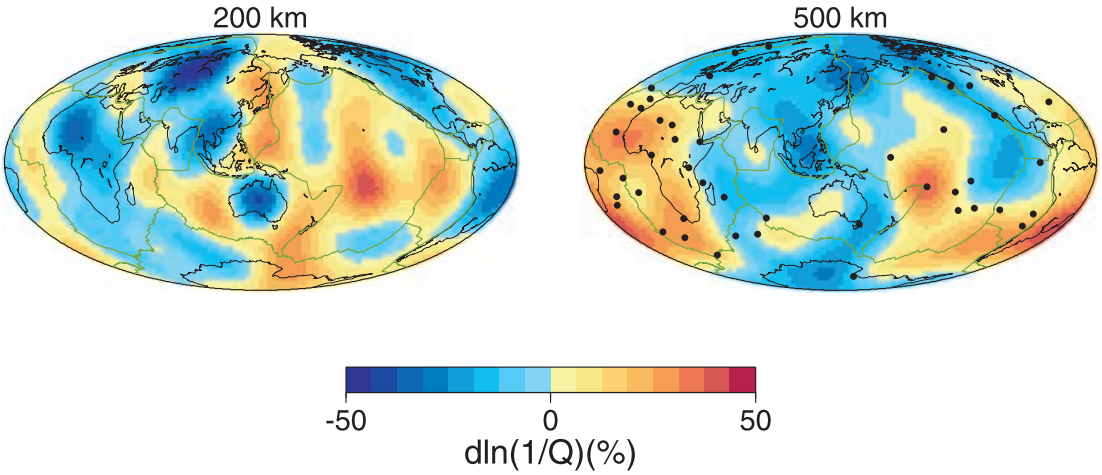

Figure 16. Degree-8 *Q* model derived with focusing effects taken into account. The same data set is used in the derivation of QRLW8, and the focusing effects are predicted by SAW24B16 and SAW16BV for Love waves and Rayleigh waves, respectively.

Gung, Y., Panning, M. & Romanowicz, B., 2003. Global anisotropy and the thickness of continents, *Nature*, **422,** 707–711.

Jackson, I., Paterson, M.S. & FitzGerald, J.D., 1992. Seismic wave dispersion and attenuation in Aheim dunite: an experimental study, *Geophys. J. Int.,* **108,** 517–534.

Jordan, T.H., 1978. A procedure for estimating lateral variations from low-frequency eigenspectra data, *Geophys. J. R. astr. Soc.,* **52,** 441–455.

Karato, S.-I., 1993. Importance of anelasticity in the interpretation of seismic tomography, *Geophys. Res. Lett.,* **20,** 1623–1626.

Karato, S.-I., 1998. A dislocation model of seismic wave attenuation and micro-creep in the earth: Harold Jeffreys and the rheology of the solid earth, *Pure appl. Geophys.,* **153,** 239–256.

Li, X.D. & Tanimoto, T., 1993. Waveforms of long-period body waves in a slightly aspherical Earth model, *Geophys. J. Int.,* **112,** 92–102.

Li, X.D. & Romanowicz, B., 1995. Comparison of global waveform inversions with and without considering cross-branch modal coupling, *Geophys. J. Int.,* **121,** 695–709(LR95).

Li, X.D. & Romanowicz, B., 1996. Global mantle shear velocity model developed using nonlinear asymptotic coupling theory, *J. geophys. Res.,* **101,** 22 245–22 272 (LR96).

Masters, G., Johnson, S., Laske, G. & Bolton, H., 1996. A shear velocity model of the mantle., *Phil. Trans. R. Soc. Lond.,* A., **354,** 1385–1411.

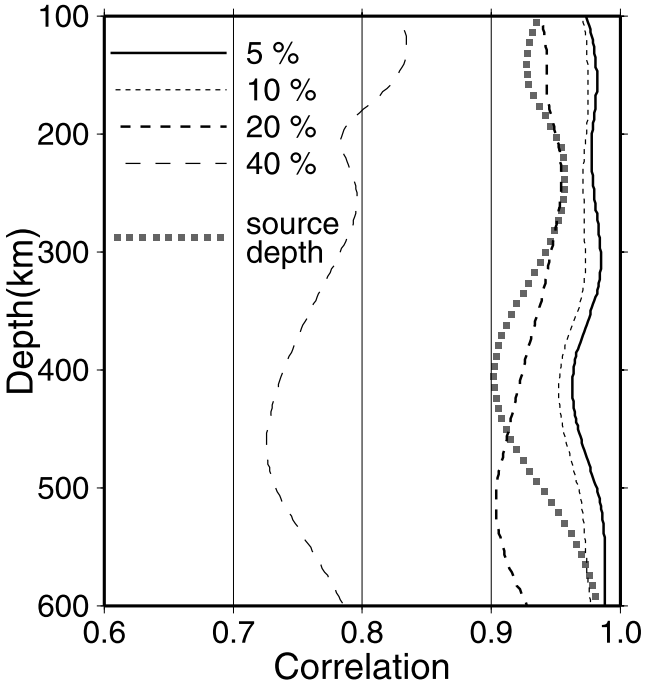

Figure 17. Correlation as a function of depth of QRLW8 and *Q* models obtained with perturbations to source parameters. The black solid and dashed lines correspond to models obtained with perturbations to moment tensors of different amplitudes. The line of grey solid squares corresponds to model obtained with perturbations to source depths. Details are given in the text.

Mégnin, C. & Romanowicz, B., 1999. The effect of theoretical formalism and data selection scheme on mantle models derived from waveform tomography, *Geophys. J. Int.,* **138,** 366–380.

Mégnin, C. & Romanowicz, B., 2000. The 3D shear velocity structure of the mantle from the inversion of body, surface and higher mode waveforms, *Geophys. J. Int.,* **143,** 709–728 (MR00).

Mitchell, B.J., 1995. Anelastic structure and evolution of the continents from seismic surface wave attenuation, *Rev. Geophys.,* **33,** 441–462.

Montagner, J.P. & Tanimoto, T., 1990. global anisotropy in the upper mantle inferred from regionalization of phase velocities, *J. geophys. Res.,* **95,** 4797–4819.

Mooney, W.D., Laske, G. & Masters, G., 1998. Crust 5.1: a global crustal model at 5 deg × 5 deg, *J. geophys. Res.,* **103,** 727–747.

Reid, F.J.L., Woodhouse, J.H. & van Heist, H.H., 2001. Upper mantle attenuation and velocity structure from measurements of differential S phases, *Geophys. J. Int.,* **145,** 615–630.

Richards, M. A., Hager, B.H. & Sleep, N.H., 1988. Dynamically supported geoid highs over hotspots: observation and theory, *J. geophys. Res.,* **93,** 7690–7708.

Romanowicz, B., 1987. Multiplet-multiplet coupling due to lateral heterogeneity: asymptotic effects on the amplitude and frequency of Earth's normal modes, *Geophys. J. R. astr. Soc.,* **90,** 75–100.

Romanowicz, B., 1990. The upper mantle degree 2: constraints and inferences from global mantle wave attenuation measurements, *J. geophys. Res.,* **95,** 11 051–11 071.

Romanowicz, B., 1994. On the measurement of Anelastic attenuation using amplitudes of low frequency surface waves, *Phys. Earth planet. Int.,* **84,** 179–191.

Romanowicz, B., 1995. A global tomographic model of shear attenuation in the upper mantle, *J. geophys. Res.,* **100,** 12 375–12 394.

Romanowicz, B., 1998. Attenuation tomography of the Earth's mantle: A review of current status, *Pure appl. Geophys.,* **153,** 257–272.

Romanowicz, B. & Gung, Y., 2002. Mega-upwellings from the core-mantle boundary to the lithosphere: implications for heat flux, *Science,* **296,** 513–516.

Romanowicz, B., Roult, G. & Kohl, T., 1987. The upper mantle degree 2 pattern: constraints from Geoscope fundamental spheroidal eigenfrequency and attenuation measurements, *Geophys. Res. Lett.,* **14,** 1219–1222.

Romanowicz, B., Gung, Y. & Capdeville, Y., 2004. Long period seismograms in a 3D earth: tests of normal mode asymptotic approximations against computations using the Spectral Element Method, in preparation.

Roth, E.G. & Wiens, D.A., 1999. Seismic attenuation tomography of the Tonga-Fuji region using phase pair methods, *J. geophys. Res.,* **104,** 4795–4809.

Roult, G., Romanowicz, B. & Montagner, J.P., 1990. 3-D upper mantle shear velocity and attenuation from fundamental mode free oscillation data, *Geophys. J. Int.,* **101,** 61–80.

Selby, N.D. & Woodhouse, J.H., 2000. Controls on Rayleigh wave amplitudes: attenuation and focusing, *Geophys. J. Int.,* **142,** 933–940.

Selby, N.D. & Woodhouse, J.H., 2002. The Q structure of the upper mantle: Constraints from Rayleigh wave amplitudes, *J. geophys. Res.,* **107**(B5), 2097, doi:10.1029/2001JB000257.

Su, W.-J., Woodward, R.L. & Dziewonski, A.M., 1994. Degree 12 model of shear velocity in the mantle, *J. geophys. Res.,* **99,** 6945–6980.

Suda, N., Shibata, N. & Fukao, Y., 1991. Degree-2 pattern of attenuation structure in the upper mantle from apparent complex frequency measurements of fundamental spheroidal modes, *Geophys. Res. Lett.,* **18,** 1119–1122.

Tanimoto, T., 1986. Free oscillation in a slightly anisotropic Earth, *Geophys. J. R. astr. Soc.,* **87,** 493–517.

Tarantola, A. & Valette, B., 1982. Generalized non-linear inverse problems solved using the least-squares criterion, *Rev. Geophys. Space Phys.,* **20,** 219–232.

van der Hilst, R.D., Widiyantoro, S. & Engdahl, E.R., 1997. Evidence for deep mantle circulation from global tomography, *Nature,* **386,** 578–584.

Vasco, D.W. & Johnson, L.R., 1998. Whole earth structure estimated from seismic arrival times, *J. geophys. Res.,* **103,** 2633–2671.

Warren, L.M. & Shearer, P.M., 2002. Mapping lateral variation in upper mantle attenuation by stacking *P* and *PP* spectra, *J. geophys. Res.,* **107**(B12), 2342, doi:10.1029/2001JB001195.

Woodhouse, J.H., 1980. The coupling and attenuation of nearly resonant multiplets in the earth's free oscillation spectrum, *Geophys. J. R. astr. Soc.,* **61,** 261–283.

Woodhouse, J.H. & Dziewonski, A.M., 1984. Mapping the upper mantle: Three-dimensional modeling of Earth structure by inversion of seismic waveforms, *J. geophys. Res.,* **89,** 5953–5986.

Zhang, Y.-S. & Tanimoto, T., 1993. High-resolution global upper mantle structure and plate tectonics, *J. geophys. Res.,* **98,** 9793–9823.